Journal of Crystal Growth 627 (2024) 127511

Contents lists available at ScienceDirect

Journal of Crystal Growth

journal homepage: www.elsevier.com/locate/jcrysgro

High-pressure crystal growth and investigation of the metal-to-metal transition of Ruddlesden–Popper trilayer nickelates $La_4Ni_3O_{10}$

Ning Yuan *, Ahmed Elghandour, Jan Arneth, Kaustav Dey, Rüdiger Klingeler

Kirchhoff Institute of Physics, Heidelberg University, 69120 Heidelberg, Germany

ARTICLE INFO

Communicated by T. Duffar

Keywords:
A1. High-pressure optical Floating zone technique
A2. Crystal structure
A2. Single crystal growth
B1. Nickelate
B2. Magnetic materials

ABSTRACT

Single crystals of Ruddlesden–Popper nickelates $La_4Ni_3O_{10}$ were grown by means of the floating-zone technique at oxygen pressure of 20 bar. Our results reveal the effects of the annealing process under pressure on the crystal structure. We present the requirements for crystal growth and show how a reported ferromagnetic impurity phase can be avoided. The different growth and post-annealing processes result in two distinct phases $P2_1/a$ and *Bmab* in which the metal-to-metal transitions occur at 152 K and 136 K, respectively.

1. Introduction

The recent discoveries of superconductivity in infinite-layer nickelates [1–8] have further demonstrated the position of nickelates as model systems to discover and decipher novel aspects of correlated electron physics. It is also the electronic similarity of the Ni^{1+} and Cu^{2+} electronic configurations which renders nickelates prime analogues to the high-T_C superconducting cuprates and has raised a surge of interest to understand and modify the critical electronic features that determine electronic correlation and in particular superconductivity in nickelates. This has brought the Ruddlesden–Popper phases $La_{n+1}Ni_nO_{3n+1}$ into the focus in which the valence of the Ni-ions and the electronic ground state can be tuned (see, e.g., [9–13]). Trilayer nickelates as reported at hand exhibit an unusual metal-to-metal transition (MMT) [14–20] with intertwined charge and spin orders developing at T_{MM} [21].

The crystal structure of Ruddlesden–Popper nickelates $R_4Ni_3O_{10}$ is commonly described as an alternating arrangement of perovskite-like layers and rock-salt-like layers [9,22] and is often regarded as quasi-two-dimensional (2D). It exhibits a mixture of Ni^{2+} and Ni^{3+} ions with an average valence of +2.67 [14]. The space group details at room temperature and ambient pressure are still controversial and the debated four different space groups are discussed specifically in Refs. [17,18,23]. By means of high-resolution synchrotron and laboratory X-ray single-crystal diffraction studies Zhang et al. concluded that the formation of the $P2_1/a$ (no. 14) and *Bmab* (no. 64) structures is closely related to the cooling rate after growth. The preparation of $La_4Ni_3O_{10}$ compounds, especially of single crystals, is challenging due to the required synthesis atmosphere of 20–30 bar oxygen pressure [9,18] and the pronounced tendency of phase mixture which is reported to be closely associated with slight variations of the oxygen content [20,24].

In this work, single crystals of $La_4Ni_3O_{10}$ were successfully grown by the high-pressure optical floating-zone method under 20 bar oxygen pressure. We investigate the different growth and post-annealing processes resulting in two different phases, i.e. $P2_1/a$ and *Bmab*, respectively, and report magnetic susceptibility and specific heat data. Our study shows sharp anomalies and marked anisotropy associated with the reported MMT in $La_4Ni_3O_{10}$. Using the here reported growth conditions avoids the formation of a previously reported ferromagnetic impurity phase.

2. Materials and experimental methods

Polycrystalline $La_4Ni_3O_{10}$ was synthesized by a standard solid-state reaction. The raw materials La_2O_3 (99.99%, Sigma-Aldrich) and NiO (99.998%, Alfa Aesar) powders were calcined at 900 °C and 1000 °C for 24 h to remove absorbed water. Stoichiometric amounts of the ingredients were mixed well in a mortar and calcined at 1050 °C for 24 h (air flow, ambient) with several intermediate grindings. The powder obtained is reground, packed in a rubber tube and isotropically pressed at 60 MPa in order to produce cylindrical rods with a length of 5–6 cm and a diameter of 5 mm as shown in Fig. 1a. The rods

* Corresponding author.
E-mail address: ning.yuan@kip.uni-heidelberg.de (N. Yuan).

https://doi.org/10.1016/j.jcrysgro.2023.127511
Received 10 October 2023; Received in revised form 20 November 2023; Accepted 25 November 2023
Available online 30 November 2023

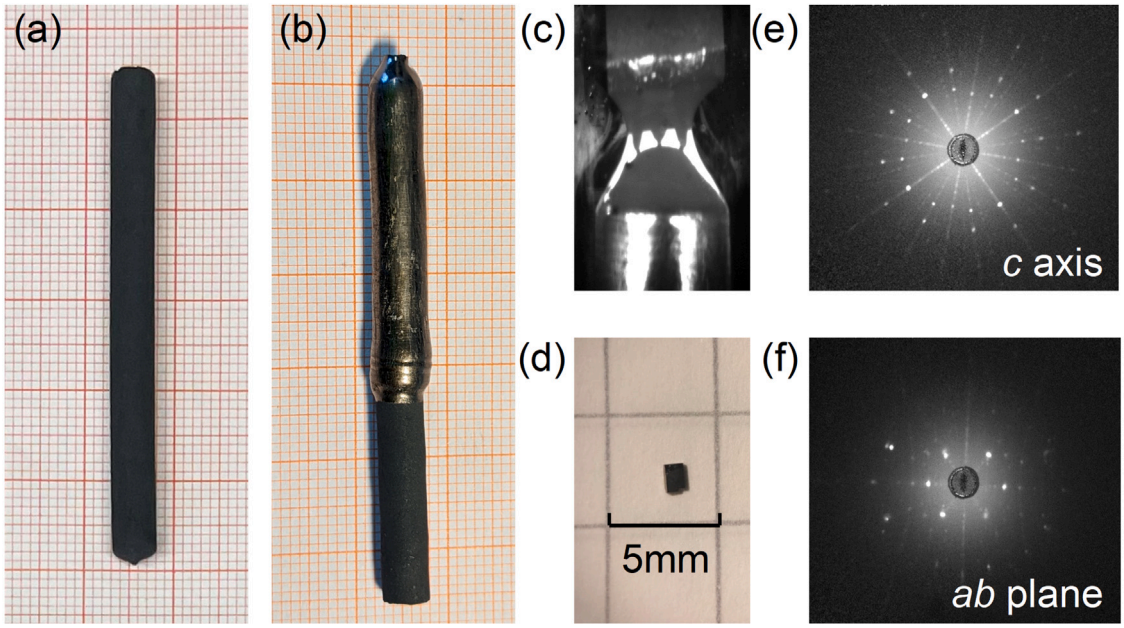

Fig. 1. ictures of (a) $La_4Ni_3O_{10}$ cylindrical polycrystalline rods, (b) the obtained $La_4Ni_3O_{10}$ boule, (c) the melting-zone formed during the growth, and (d) the oriented and cut single crystal used for magnetic and calorimetric measurements. (e,f) Laue patterns of the $La_4Ni_3O_{10}$ single crystal oriented along *c* axis and *ab* plane, respectively.

were annealed for 24 h at 1400 °C. It is notable that according to the thermodynamic analysis of the La-Ni-O system [25,26], only La_2NiO_4 compounds can be synthesized at ambient pressure, and our experimental results are consistent with it. Single crystals of $La_4Ni_3O_{10}$ were then successfully grown using the high-pressure optical floating-zone furnace (HKZ, SciDre) [27]. We employed a 5 kw Xenon arc lamp as the heat source, and 20 bar O_2 atmosphere with an O_2 flow rate maintained at 0.1 l/min. The volume of the HKZ inner sample chamber is approximately 23 ml. The composition of feed and seed rods are identical, both are polycrystalline $La_4Ni_3O_{10}$. To improve the homogeneity of the melting zone, counter-rotation of the feed and seed rods at 10 rmp is necessary. The feed rod was pulled at 6 mm/h and the seed rod was pulled at 4 mm/h to maintain the zone stability. Using an in-situ temperature measurement by means of a two-color pyrometer [28,29], the temperature of the melting zone during growth was determined to about 1650 °C. After the initial growth we performed a rapid cooling of the melting zone to avoid the precipitation of oxygen. In addition to crystals obtained from pristine boules grown as described above and further on labelled 'S1', we also applied a post-annealing procedure resulting in crystals labelled 'S2'. The post-annealing was carried out in the HKZ furnace where the sample is held under the 20 bar oxygen pressure at 950 °C for 2 h, then quenched to room temperature following Ref. [18]. The latter process was achieved by quickly removing the rod out of focus.

The phase purity and crystallinity of the resulting materials were studied by powder X-ray diffraction (XRD) and the back-reflection Laue method. XRD was performed at room temperature by means of a Bruker D8 Advance ECO diffractometer using Cu-Kα radiation (λ = 1.5418 Å). Data have been collected in the 2Θ range of 10–90° with 0.02° step-size. Laue diffraction was done on a high-resolution X-ray Laue camera (Photonic Science). Magnetic studies in the temperature regime 1.8–350 K have been performed in a SQUID magnetometer (MPMS3, Quantum Design Inc.) following either field-cooled (FC) or zero-field-cooled (ZFC) protocols where the sample has been cooled down to lowest temperature in the actual measurement field or in zero magnetic field, respectively, before applying the external magnetic field at lowest temperature. Measurements of the specific heat have been performed in a Physical Properties Measurement System (PPMS, Quantum Design Inc.) utilizing a relaxation method.

3. Results

3.1. Single crystal growth

$La_4Ni_3O_{10}$ single crystals were successfully grown under 20 bar oxygen pressure (see Fig. 1b for a picture of the as-grown boule). In order to maintain a stable melting zone, the feed rod must be pulled faster than the seed rod; optimized feed and seed rod velocities chosen for the experiment were 6 mm/h and 4 mm/h, respectively. The melting zone formed during the successful growth is shown in Fig. 1c. Using the same velocities for both rods resulted in the depletion of liquid in the melting zone, somehow similar as observed for $LaNiO_3$ [28]. The inconsistent velocity setting results in wider diameter of the as-grown single crystal compared to the feed (see Fig. 1b) and in general entails a larger potential for cracking.

The procedure yields shiny boules from which single crystalline grains have been obtained, oriented, and cut (Fig. 1b and d). Crystals were obtained from both the pristine boule (S1) and the annealed one (S2). Figs. 1d-f show the oriented and cut crystal S2 as well as back-reflection Laue images obtained along the *c* axis and the *ab* plane, respectively. Similar sample dimension and Laue patterns have been obtained for crystal S1.

Powder X-ray diffraction was performed on several ground single crystals taken from the very vicinity of the oriented single crystal bulks in order to study phase purity of the grown single crystals. The resulting room temperature XRD pattern as well as the Rietveld refinements to the data presented in Fig. 2a,b indicate that the main phase is $La_4Ni_3O_{10}$. In addition, we observe a few Bragg peaks that do not correspond to $La_4Ni_3O_{10}$ phases but are assigned to $La_3Ni_2O_7$ impurities. We find that the annealing procedure under oxygen pressure leads to a notable reduction of the impurity phase, as shown in Fig. 2c,d.

3.2. Magnetization

The in-plane and out-of-plane magnetization measurements performed on single crystal samples S1 and S2 shown in Fig. 3 provide further information on the quality of the single crystals and on potential impurity phases. The main features are sharp jumps or kinks in the static susceptibility $\chi = M/B$ at T_{MM}^{Bmab} = 152 K and $T_{MM}^{P2_1/a}$ = 136 K

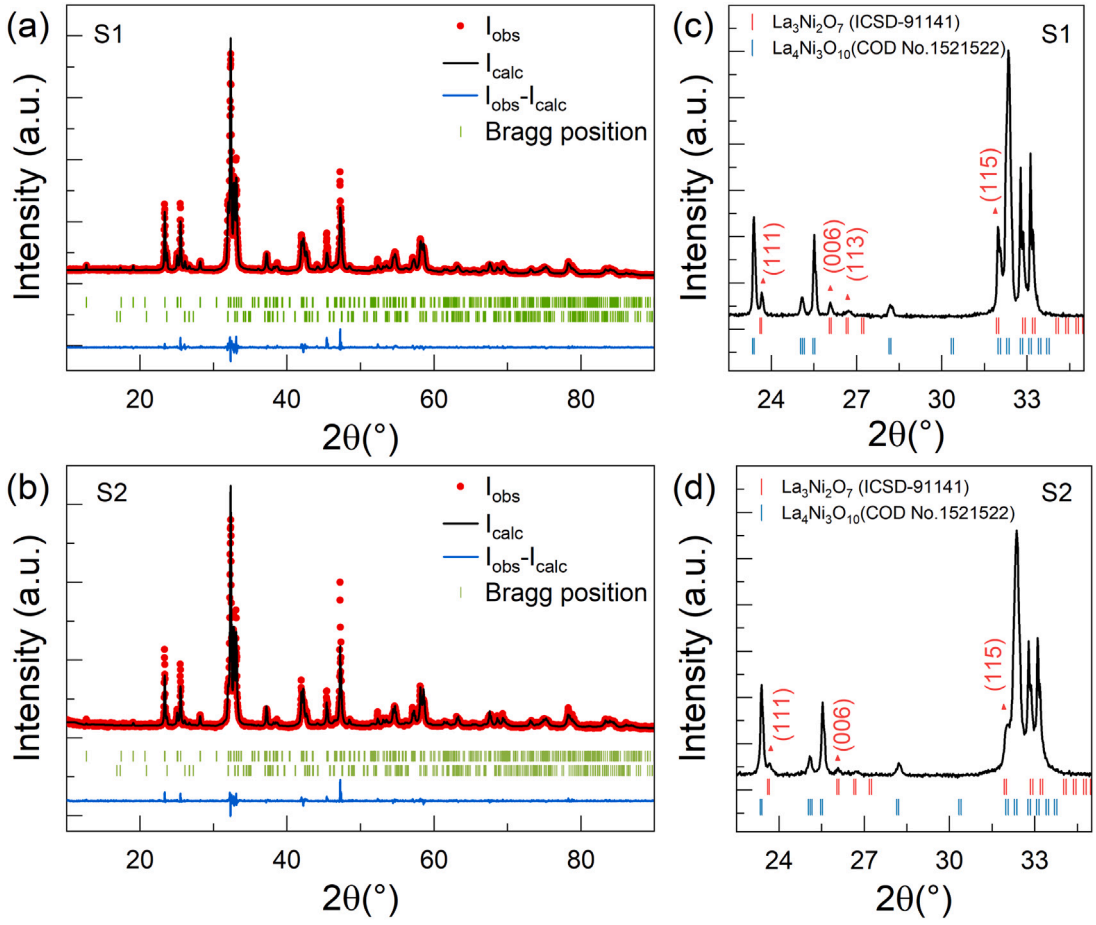

Fig. 2. Room temperature powder XRD patterns and corresponding Rietveld refinement [30] of ground $La_4Ni_3O_{10}$ single crystals grown at 20 bar O_2 pressure. S1 (a,c) and S2 (b,d) show results for pristine and annealed crystals, respectively (see the text). The observed diffraction pattern is shown in red, the calculated one in black, and the difference between them is shown in blue. The vertical green bars show the expected Bragg positions of $La_4Ni_3O_{10}$ (COD no. 7237332 [31]) and $La_3Ni_2O_7$ (ICSD no. 91141 [31]). The refinement converged to R_p = 15.9%, R_{wp} = 16.2%, χ^2 = 5.7 for S1 and R_p = 27.2%, R_{wp} = 24.8%, χ^2 = 3.7 for S2. (For interpretation of the references to colour in this figure legend, the reader is referred to the web version of this article.)

for the pristine S1 and the annealed S2, respectively. This result is consistent with previous reports [15–19,21,32] which imply that the MMT is characterized by an intertwined charge-magnetic ordering phenomenon.

We emphasize the absence of FC/ZFC hysteresis behaviour in the 1.8 to 350 K temperature interval (see Fig. 3); previously reported crystals show a pronounced anomaly in the susceptibility at around 50 K and strong differences between FC and ZFC susceptibilities, suggesting an unknown ferromagnetic component [18]. This component is absent in our crystals which confirms its extrinsic nature.[1] The absence of ferromagnetic impurities in our crystals is further confirmed by isothermal magnetization studies (see Fig. 4).

Despite the challenges and controversy regarding the determination of crystal structure of $La_4Ni_3O_{10}$ by powder XRD analysis [17,18,23], the magnetic susceptibility data not only imply phase purity with respect to magnetic impurity phases, but also strongly suggest that the pristine crystal S1 exhibits *Bmab* structure while S2 exhibits $P2_1/a$ structure. In particular, the very pronounced and sharp single anomalies exclude mixing of both phases in either of the single crystals. The very sharp jump in χ_c at T_{MM} in S2 in particular indicates excellent crystallinity of the $P2_1/a$ phase crystal. Zhang et al. [18] have identified the postgrowth cooling rate as a crucial parameter for obtaining a thermodynamically stable phase. The reported experiments on biphasic $La_4Ni_3O_{10}$ crystals suggest that the *Bmab* structure can be transformed to $P2_1/a$. In our experiments we have performed rapid cooling of the as-grown boule as well as further high-pressure annealing. Our results show that the phase pure *Bmab* structure forms after rapid cooling while it completely transforms to $P2_1/a$ upon heat treatment confirming the latter being the thermodynamically stable phase.

In general, the susceptibility data in Fig. 3 show (1) the continuous decrease of χ upon cooling from 350 K towards T_{MM}, with a minimum in χ_c at T_{MM} and a broad minimum in χ_{ab} slightly below. (2) Pronounced anisotropy in the whole temperature range under study with χ_{ab}/χ_c= 1.42 (S1) respectively 1.28 (S2), at 350 K. (3) A Curie–Weiss-like (CW-like) increase of the magnetic susceptibility $\chi(T)$ at low temperatures which qualitatively corresponds to a Brillouin-like contribution to $M(B, T = 2\ \mathrm{K})$ (see Fig. 4 below).

Notably, the seemingly CW-like behaviour of magnetic susceptibility in both the $P2_1/a$ (S1) and *Bmab* (S2) systems well below T_{MM} (see Fig. 3) cannot be described well in terms of the extended CW law $\chi(T) = \frac{C}{T+\Theta} + \chi_0$, with C the Curie constant, Θ the Weiss temperature, and a temperature independent term χ_0, in an extended temperature regime. This implies that at least one or even all these parameters change upon cooling. In an attempt to quantify these parameters at low temperature by restricting the CW fit to $T < 10$ K, the data are reasonably well described by the parameters listed in Table 1. The small values of Θ imply the presence of very weakly coupled magnetic moments. When evaluating the Curie constant by assuming magnetic moments $S = 1$ and $g \simeq 2$, the data suggest 0.4 ‰/f.u. of such

[1] Within the error bars of the experiment, we obtain an upper limit of the ferromagnetic component being 25 times less than in Ref. [18].

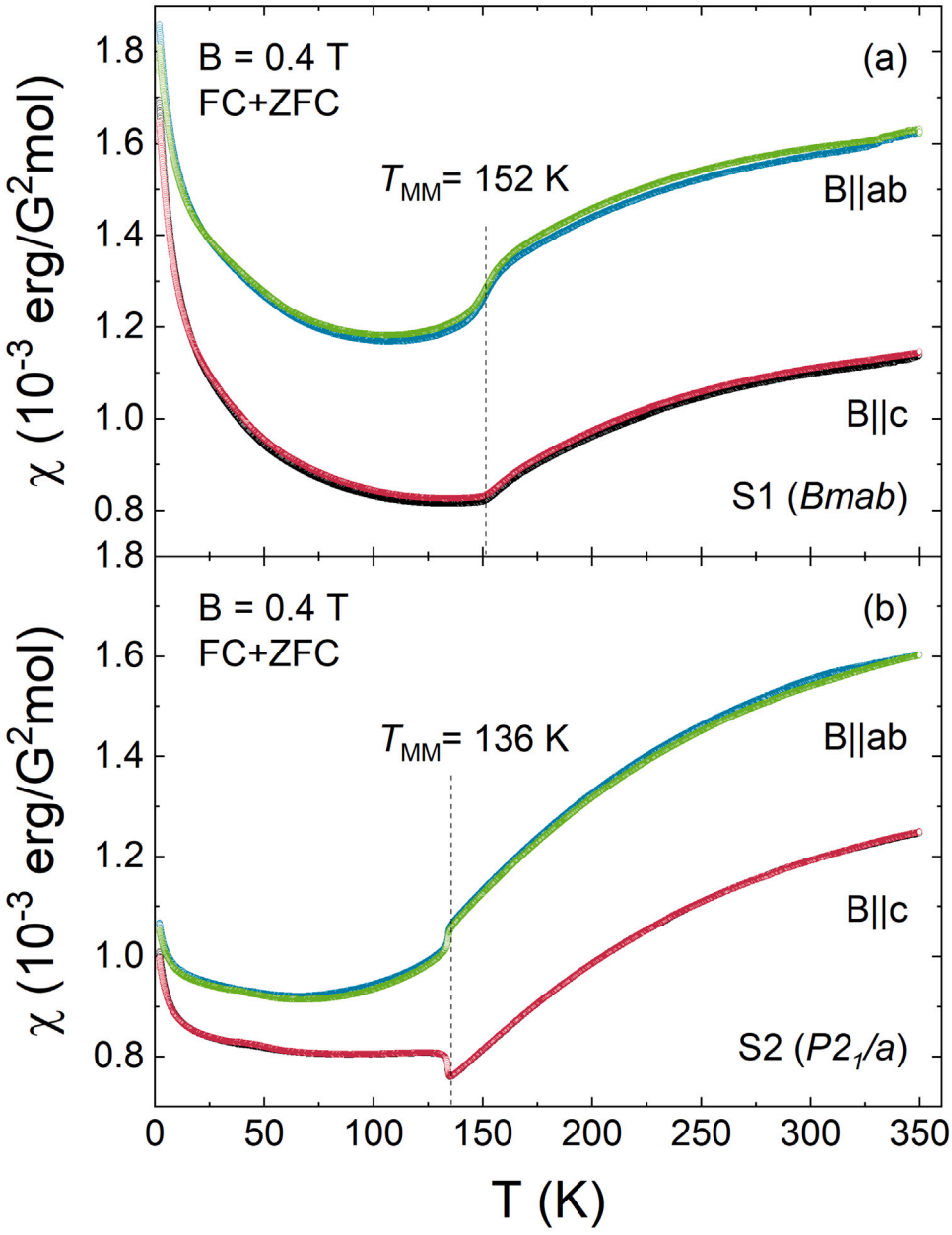

Fig. 3. Static magnetic susceptibility $\chi = M/B$ vs. T measured at $B = 0.4$ T of (a) the pristine crystal (S1:*Bmab*) and (b) the annealed crystal (S2: $P2_1/a$). For each field direction ($B \parallel c$ and $B \parallel ab$) both fc and zfc data are presented but do not show visible differences.

moments. The observed $\chi(T)$ however also implies that the number of localized moments, their magnetic interaction and/or χ_0 change with temperature.

The isothermal magnetization (Fig. 4) shows rather linear behaviour in the high-field regime but also clear signatures of quasi-free spins as there is distinct right-bending in small fields. We attribute the linear behaviour to the response of the main magnetic phase. Considering these contributions, $M(B)$ at $T = 2$ K may be described by

$$M(B) = M_s \times B_S\left(\frac{g\mu_B S B}{k_B T}\right) + \chi_0 B. \quad (1)$$

Here, M_s is the saturation magnetization of the quasi-free moments, B_S the Brillouin function, S spin, k_B Boltzmann constant, μ_B Bohr magneton, g the g-factor, and χ_0 the linear slope. Fitting the data yields the results listed in Table 1. The number of quasi-free spins obtained from this analysis through the parameter M_s is again in the $\lesssim 1$ ‰-regime if assuming localized moments with $S = 1$. The obtained values of χ_0 are rather high with respect to the bare Sommerfeld model: Using $\gamma = 14.5(13.3)$ mJ/(mol K²) for the *Bmab* ($P2_1/a$) structured material [18], for non-correlated conduction electrons, one obtains $\chi_P^{Bmab} \simeq 2.0\times10^{-4}$ erg/(G²mol) ($\chi_P^{P2_1/a} \simeq 1.8\times10^{-4}$ erg/(G²mol)). Strong anisotropy of $\partial M/\partial B$, at $B = 7$ T, already implies that magnetism of conduction electrons is however only one component determining the magnetic response in $La_4Ni_3O_{10}$.

3.3. Specific heat and $\partial T_{MM}/\partial B$

The specific heat of the single crystals under study shown in Figs. 5 and 6 confirms significant anomalous entropy changes at T_{MM}. While the anomaly of the $P2_1/a$ structured crystal is typical for a first order transition, we conclude from the shape of the anomaly observed for the *Bmab* structure the discontinuous character of the MMT, too (see Fig. 5b). In an attempt to quantify the entropy changes ΔS_{MM} associated with the MMT, a polynomial background was fitted to the data well below and above the specific heat anomaly as shown in Fig. 5a and

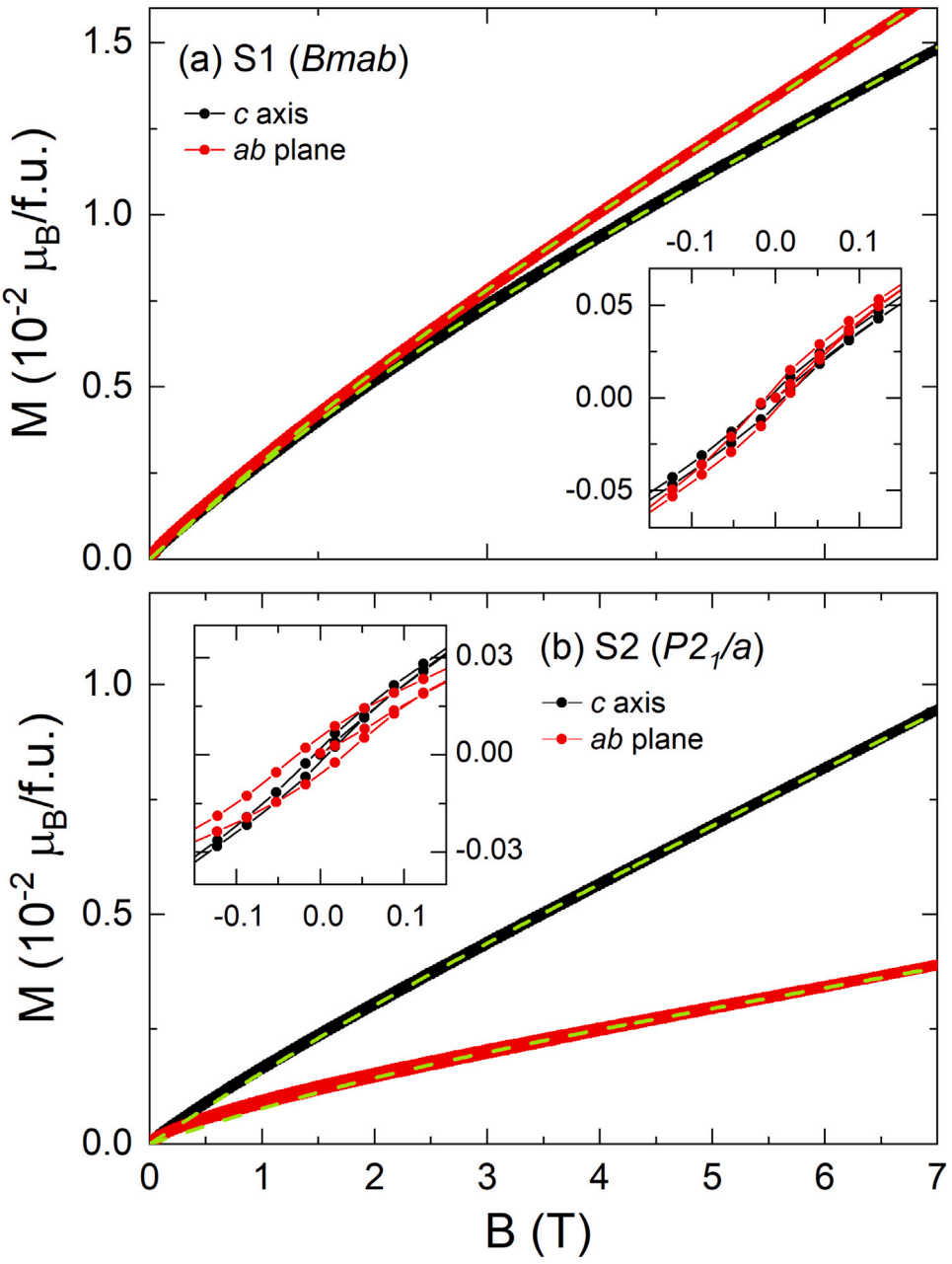

Fig. 4. Isothermal magnetization of (a) the pristine crystal (S1:*Bmab*) and (b) the annealed crystal (S2: $P2_1/a$), at $T = 2$ K, for $B \parallel c$ and $B \parallel ab$ (both up- and down-sweeps are shown). Dashed lines extrapolate the linear high-field behaviour from which χ_c and χ_{ab} in Table 1 are derived. Insets: M vs. B for -0.15 T $\leq B \leq$ 0.15 T. For a full $M(B)$ curve ranging from -7 T to $+7$ T see the Supplemental Material [33].

Table 1
Fitting magnetization data in Figs. 3 and 4 (see the text). M_s and χ are saturation magnetization of the quasi-free spins and linear slope derived from $M(B, T = 2\ \text{K})$. C, Θ, and χ_0 are the Curie constant, Weiss temperature and temperature-independent susceptibility from fitting $M(T)/B$ at $T < 10$ K.

	M_s^c μ_B/f.u.	χ_c erg/(G^{2}mol)	C erg K/(G^{2}mol)	Θ K	χ_0 erg/(G^{2}mol)	M_s^{ab} μ_B/f.u.	χ_{ab} erg/(G^2 mol)	C erg K/(G^2 mol)	Θ K	χ_0 erg/(G^2 mol)
S1(*Bmab*)	2.2×10^{-3}	3.2×10^{-3}	10×10^{-3}	9	8×10^{-4}	1.8×10^{-3}	3.8×10^{-3}	6×10^{-3}	7	1.2×10^{-3}
S2($P2_1/a$)	7.8×10^{-4}	2.2×10^{-3}	1.1×10^{-3}	3	8×10^{-4}	8.2×10^{-4}	7.7×10^{-4}	7×10^{-4}	3	8×10^{-4}

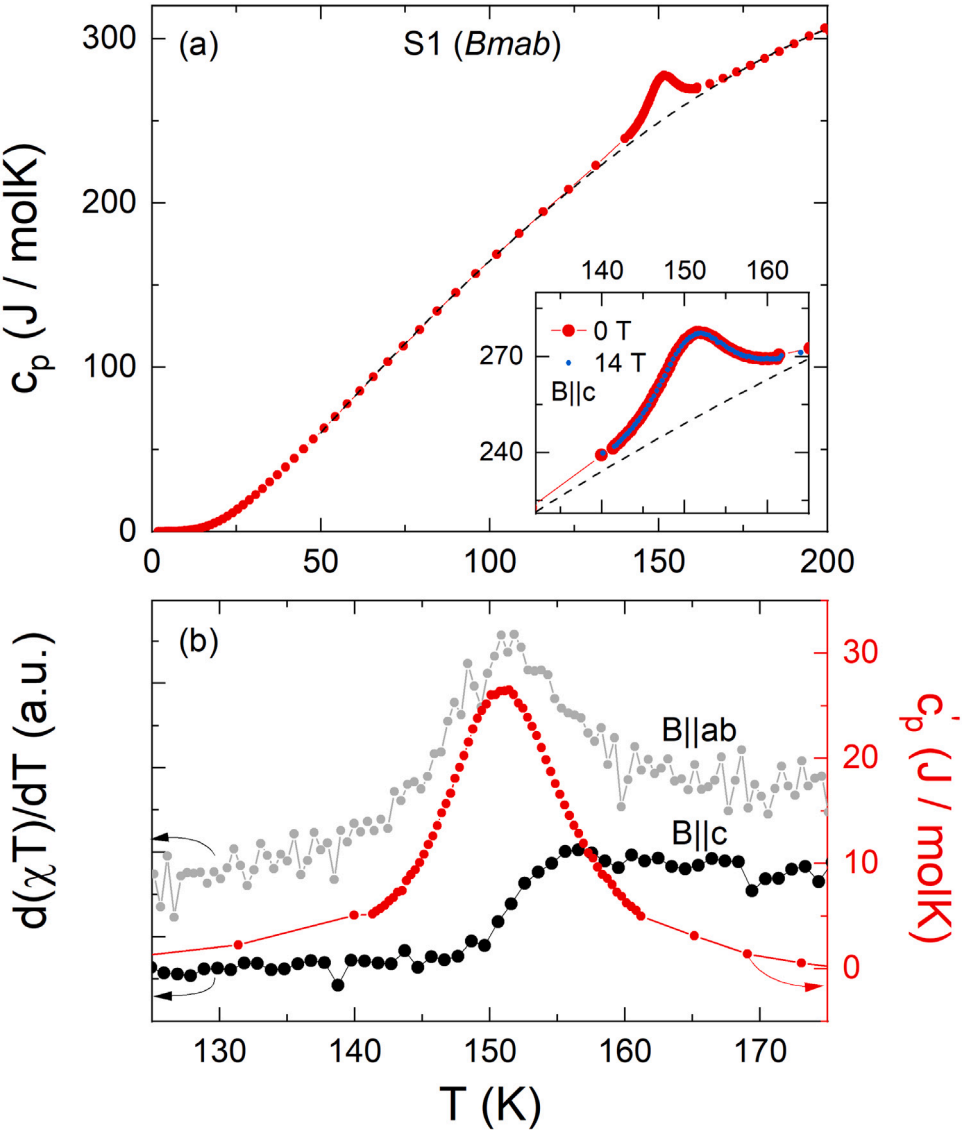

Fig. 5. (a) Specific heat capacity of the pristine crystal (S1:*Bmab*). (b) Fisher's specific heat $\partial(\chi T)/\partial T$ and anomalous contributions to the specific heat c_p' obtained by subtracting a polynomial background from the data (dashed line in (a)).

6a [34]. The background mainly reflects the phonon contribution. Due to the large size of the anomaly, using different temperature ranges for the determination of the background and/or choosing different fit functions does not change the result significantly. Subtracting the obtained background from the data yields the anomaly contribution to the specific heat c_p' as shown in Fig. 5b and 6b. Integrating c_p'/T yields the entropy changes ΔS_{MM} listed in Table 2.

Our analysis implies that for both structures, *Bmab* and $P2_1/a$, the metal-to-metal transition is associated with similar entropy changes. The data also enable us to conclude about the field dependence of T_{MM} by exploiting the Clausius–Clapeyron equation

$$\frac{\partial T_{MM}}{\partial B} = -\frac{\Delta M}{\Delta S}. \quad (2)$$

Using the experimentally obtained jumps in M and S yields insignificant effects of magnetic fields on T_{MM} (see Table 2) which is experimentally confirmed by our measurements of the specific heat at $B \parallel c = 14$ T (see the insets in Fig. 5a and 6a).

The obtained entropy changes are by ca. 20 % smaller than found for single crystal reported in Ref. [18] and ca. 40 % larger than recently determined from a $P2_1/a$-structured polycrystal [17]. A comparison of the anomalies is shown in Fig. 7. The data also imply slightly different ordering temperatures T_{MM} which is by 4.5 K lower for *Bmab* and 2.6 K larger for $P2_1/a$ in Ref. [18] than found in our crystals. T_{MM} of the polycrystal perfectly agrees to our single crystal result [17]. These slight differences may be due to oxygen stoichiometry, which is considered a key parameter of electronic properties [24]. The fact that the specific heat and magnetic susceptibility anomalies at least for the $P2_1/a$ system are much sharper in our crystal as compared to reported anomalies may be regarded as an indication that the crystals have particular excellent crystallinity.

Table 2
Changes in entropy (ΔS_{MM}), magnetization (ΔM, and $\Delta(\partial M/\partial T)_{MM}$) at the MMT and field dependencies of T_{MM} calculated by means of Eq. (2) .

	S1 (*Bmab*)	S2 ($P2_1/a$)
ΔS_{MM} (J/(mol K))	1.4(1)	1.6(1)
ΔM^c_{MM} (10^{-3}erg/(G^2 mol))	–	0.05(1)
$\Delta(\partial M/\partial T)^c_{MM}$ (erg/G^2 mol K))	–	0.006
ΔM^{ab}_{MM} (10^{-3}erg/(G^2 mol))	−0.15(2)	−0.05(1)
$\lvert\partial T^{ab}_{MM}/\partial B\rvert$ (mK/T)	<0.01	<0.003

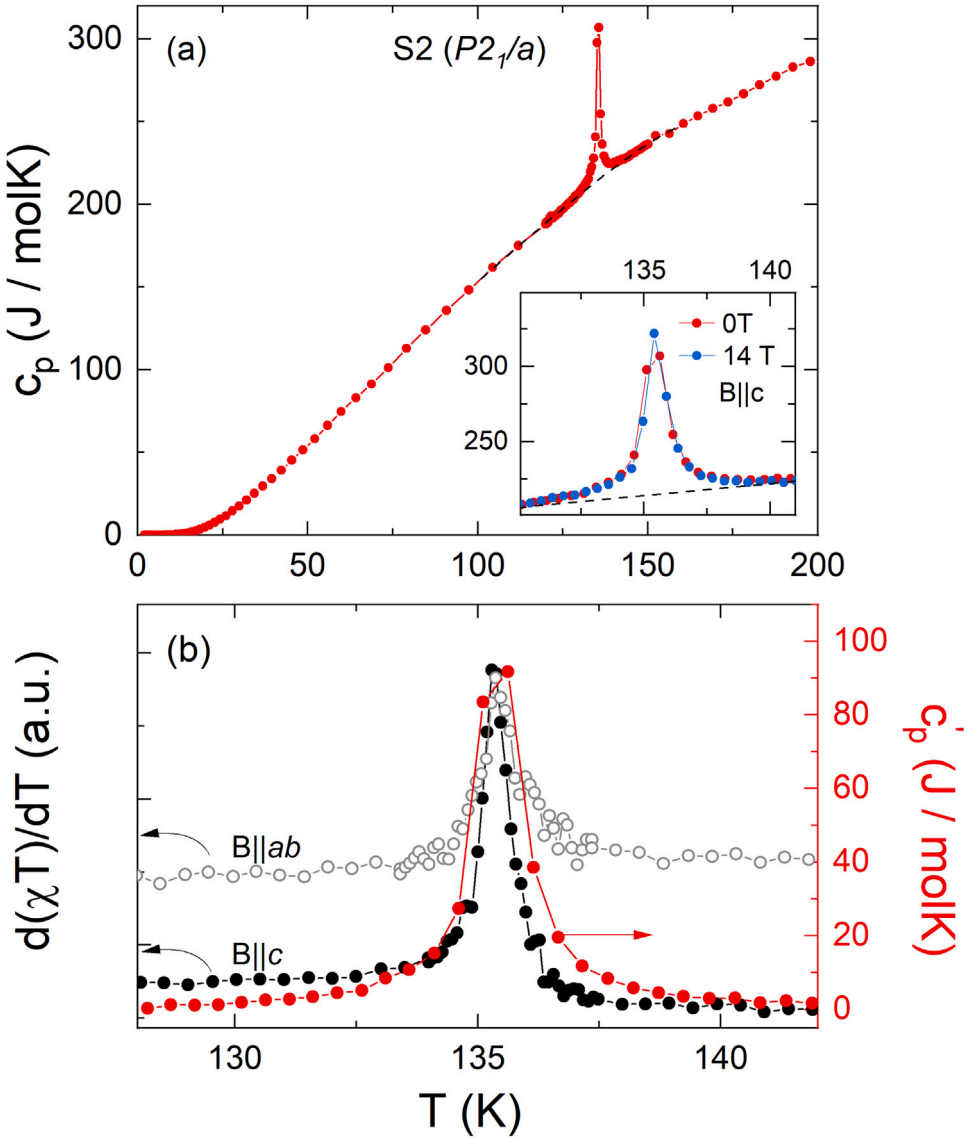

Fig. 6. (a) Specific heat capacity of the annealed crystal (S2: $P2_1/a$). (b) Fisher's specific heat $\partial(\chi T)/\partial T$ and anomalous contributions to the specific heat c'_p obtained by subtracting a polynomial background from the data (dashed line in (a)).

4. Summary

$La_4Ni_3O_{10}$ single crystals were successfully grown and subsequently annealed at 20 bar oxygen pressure. Our specific heat and magnetization measurements imply $P2_1/a$ and *Bmab* structured crystals, respectively, in which the metal-to-metal transitions occur at 152 K and 136 K. Sharp anomalies in the response functions imply highly crystalline samples and the thermodynamic and magnetic properties are analysed.

CRediT authorship contribution statement

Ning Yuan: Data curation, Writing – original draft. **Ahmed Elghandour:** Data curation. **Jan Arneth:** Data curation. **Kaustav Dey:** Methodology. **Rüdiger Klingeler:** Project administration, Supervision, Writing – review & editing.

Declaration of competing interest

The authors declare that they have no known competing financial interests or personal relationships that could have appeared to influence the work reported in this paper.

Data availability

Data will be made available on request.

Acknowledgements

The authors thank Ilse Glass for technical support. Support by the Deutsche Forschungsgemeinschaft (DFG), Germany under Germany's Excellence Strategy+ EXC2181/1-390900948 (The Heidelberg STRUCTURES Excellence Cluster) and through project KL1824/13-1 is gratefully acknowledged. N.Y. acknowledges fellowship by the Chinese Scholarship Council (File No. 201906890005).

Appendix A. Supplementary data

Supplementary material related to this article can be found online at https://doi.org/10.1016/j.jcrysgro.2023.127511. It contains the isothermal magnetization M *vs.* B of the pristine crystal (*Bmab*) and the annealed crystal ($P2_1/a$), at $T = 2$ K and -7 T $\leq B \leq 7$ T for $B \parallel c$ and $B \parallel ab$.

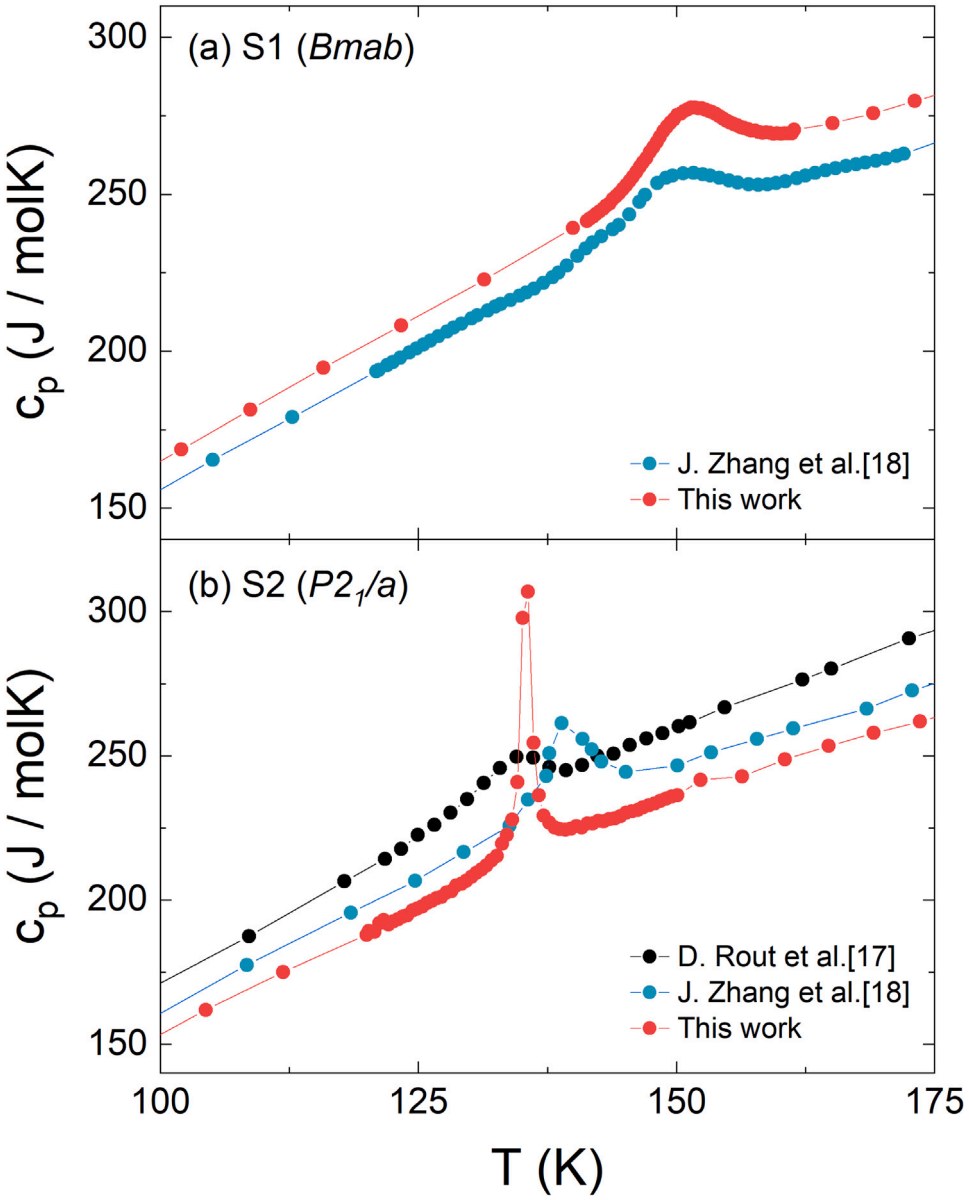

Fig. 7. Comparison of specific heat capacity of (a) the pristine crystal (S1: *Bmab*) and (b) the annealed crystal (S2: $P2_1/a$) with single crystal [18] and polycrystal [17] data reported in the literature.

References

[1] D. Li, K. Lee, B.Y. Wang, M. Osada, S. Crossley, H.R. Lee, Y. Cui, Y. Hikita, H.Y. Hwang, Superconductivity in an infinite-layer nickelate, Nature 572 (7771) (2019) 624–627.

[2] D. Li, B.Y. Wang, K. Lee, S.P. Harvey, M. Osada, B.H. Goodge, L.F. Kourkoutis, H.Y. Hwang, Superconducting dome in $Nd_{1-x}Sr_xNiO_2$ infinite layer films, Phys. Rev. Lett. 125 (2) (2020) 027001.

[3] S. Zeng, C.S. Tang, X. Yin, C. Li, M. Li, Z. Huang, J. Hu, W. Liu, G.J. Omar, H. Jani, et al., Phase diagram and superconducting dome of infinite-layer $Nd_{1-x}Sr_xNiO_2$ thin films, Phys. Rev. Lett. 125 (14) (2020) 147003.

[4] Q. Gu, Y. Li, S. Wan, H. Li, W. Guo, H. Yang, Q. Li, X. Zhu, X. Pan, Y. Nie, et al., Single particle tunneling spectrum of superconducting $Nd_{1-x}Sr_xNiO_2$ thin films, Nat. Commun. 11 (1) (2020) 6027.

[5] M. Osada, B.Y. Wang, B.H. Goodge, K. Lee, H. Yoon, K. Sakuma, D. Li, M. Miura, L.F. Kourkoutis, H.Y. Hwang, A superconducting praseodymium nickelate with infinite layer structure, Nano Lett. 20 (8) (2020) 5735–5740.

[6] M. Osada, B.Y. Wang, K. Lee, D. Li, H.Y. Hwang, Phase diagram of infinite layer praseodymium nickelate $Pr_{1-x}Sr_xNiO_2$ thin films, Phys. Rev. Mater. 4 (12) (2020) 121801.

[7] M. Osada, B.Y. Wang, B.H. Goodge, S.P. Harvey, K. Lee, D. Li, L.F. Kourkoutis, H.Y. Hwang, Nickelate superconductivity without rare-earth magnetism: (La, Sr)NiO_2, Adv. Mater. 33 (45) (2021) 2104083.

[8] S. Zeng, C. Li, L.E. Chow, Y. Cao, Z. Zhang, C.S. Tang, X. Yin, Z.S. Lim, J. Hu, P. Yang, et al., Superconductivity in infinite-layer nickelate $La_{1-x}Ca_xNiO_2$ thin films, Sci. Adv. 8 (7) (2022) eabl9927.

[9] M. Greenblatt, Ruddlesden-Popper $Ln_{n+1}Ni_nO_{3n+1}$ nickelates: structure and properties, Curr. Opin. Solid State Mater. Sci. 2 (2) (1997) 174–183.

[10] H. LaBollita, A.S. Botana, Electronic structure and magnetic properties of higher-order layered nickelates: $La_{n+1}Ni_nO_{2n+2} (n = 4 - 6)$, Phys. Rev. B 104 (2021) 035148.

[11] M.-C. Jung, J. Kapeghian, C. Hanson, B. Pamuk, A.S. Botana, Electronic structure of higher-order Ruddlesden-Popper nickelates, Phys. Rev. B 105 (2022) 085150.

[12] G.A. Pan, Q. Song, D. Ferenc Segedin, M.-C. Jung, H. El-Sherif, E.E. Fleck, B.H. Goodge, S. Doyle, D. Córdova Carrizales, A.T. N'Diaye, P. Shafer, H. Paik, L.F. Kourkoutis, I. El Baggari, A.S. Botana, C.M. Brooks, J.A. Mundy, Synthesis and electronic properties of $Nd_{n+1}Ni_nO_{3n+1}$ Ruddlesden-Popper nickelate thin films, Phys. Rev. Mater. 6 (2022) 055003.

[13] J. Zhang, A. Botana, J. Freeland, D. Phelan, H. Zheng, V. Pardo, M. Norman, J. Mitchell, Large orbital polarization in a metallic square-planar nickelate, Nat. Phys. 13 (9) (2017) 864–869.

[14] S. Kumar, Ø. Fjellvåg, A.O. Sjåstad, H. Fjellvåg, Physical properties of Ruddlesden–Popper (n = 3) nickelate: $La_4Ni_3O_{10}$, J. Magn. Magn. Mater. 496 (2020) 165915.

[15] B.-Z. Li, C. Wang, P. Yang, J. Sun, Y.-B. Liu, J. Wu, Z. Ren, J.-G. Cheng, G.-M. Zhang, G.-H. Cao, Metal-to-metal transition and heavy-electron state in $Nd_4Ni_3O_{10-\delta}$, Phys. Rev. B 101 (19) (2020) 195142.
[16] S. Huangfu, G.D. Jakub, X. Zhang, O. Blacque, P. Puphal, E. Pomjakushina, F.O. von Rohr, A. Schilling, Anisotropic character of the metal-to-metal transition in $Pr_4Ni_3O_{10}$, Phys. Rev. B 101 (10) (2020) 104104.
[17] D. Rout, S.R. Mudi, M. Hoffmann, S. Spachmann, R. Klingeler, S. Singh, Structural and physical properties of trilayer nickelates $R_4Ni_3O_{10}$ (R = La, Pr, and Nd), Phys. Rev. B 102 (19) (2020) 195144.
[18] J. Zhang, H. Zheng, Y.-S. Chen, Y. Ren, M. Yonemura, A. Huq, J. Mitchell, High oxygen pressure floating zone growth and crystal structure of the metallic nickelates $R_4Ni_3O_{10}$ (R = La,Pr), Phys. Rev. Mater. 4 (8) (2020) 083402.
[19] S. Huangfu, X. Zhang, A. Schilling, Correlation between the tolerance factor and phase transition in $A_{4-x}B_xNi_3O_{10}$ (A and B = La, Pr, and Nd; x = 0, 1, 2, and 3), Phys. Rev. Res. 2 (3) (2020) 033247.
[20] G. Wu, J. Neumeier, M. Hundley, Magnetic susceptibility, heat capacity, and pressure dependence of the electrical resistivity of $La_3Ni_2O_7$ and $La_4Ni_3O_{10}$, Phys. Rev. B 63 (24) (2001) 245120.
[21] J. Zhang, D. Phelan, A. Botana, Y.-S. Chen, H. Zheng, M. Krogstad, S.G. Wang, Y. Qiu, J. Rodriguez-Rivera, R. Osborn, et al., Intertwined density waves in a metallic nickelate, Nat. Commun. 11 (1) (2020) 6003.
[22] Z. Zhang, M. Greenblatt, Synthesis, structure, and properties of $Ln_4Ni_3O_{10-\delta}$ (Ln = La, Pr, and Nd), J. Solid State Chem. 117 (2) (1995) 236–246.
[23] D. Puggioni, J.M. Rondinelli, Crystal structure stability and electronic properties of the layered nickelate $La_4Ni_3O_{10}$, Phys. Rev. B 97 (11) (2018) 115116.
[24] M. Carvalho, M. Cruz, A. Wattiaux, J. Bassat, F. Costa, M. Godinho, Influence of oxygen stoichiometry on the electronic properties of $La_4Ni_3O_{10\pm\delta}$, J. Appl. Phys. 88 (1) (2000) 544–549.
[25] M. Zinkevich, N. Solak, H. Nitsche, M. Ahrens, F. Aldinger, Stability and thermodynamic functions of lanthanum nickelates, J. Alloys Compd. 438 (1–2) (2007) 92–99.
[26] M. Zinkevich, F. Aldinger, Thermodynamic analysis of the ternary La-Ni-O system, J. Alloys Compd. 375 (1–2) (2004) 147–161.
[27] C. Neef, H. Wadepohl, H.-P. Meyer, R. Klingeler, High-pressure optical floating-zone growth of Li(Mn, Fe)PO_4 single crystals, J. Cryst. Growth 462 (2017) 50–59.
[28] K. Dey, W. Hergett, P. Telang, M.M. Abdel-Hafiez, R. Klingeler, Magnetic properties of high-pressure optical floating-zone grown $LaNiO_3$ single crystals, J. Cryst. Growth 524 (2019) 125157.
[29] W. Hergett, C. Neef, H. Wadepohl, H.-P. Meyer, M.M. Abdel-Hafiez, C. Ritter, E. Thauer, R. Klingeler, High-pressure optical floating-zone growth of Li_2FeSiO_4 single crystals, J. Cryst. Growth 515 (2019) 37–43.
[30] J. Rodríguez-Carvajal, An Introduction to the Program FullProf 2000 (Version July 2001), 2001.
[31] C.D. Ling, D.N. Argyriou, G. Wu, J. Neumeier, Neutron diffraction study of $La_3Ni_2O_7$: Structural relationships among n = 1, 2, and 3 phases $La_{n+1}Ni_nO_{3n+1}$, J. Solid State Chem. 152 (2) (2000) 517–525.
[32] H. Li, X. Zhou, T. Nummy, J. Zhang, V. Pardo, W.E. Pickett, J.F. Mitchell, D.S. Dessau, Fermiology and electron dynamics of trilayer nickelate $La_4Ni_3O_{10}$, Nat. Commun. 8 (1) (2017) 704.
[33] N. Yuan, A. Elghandour, J. Arneth, R. Klingeler, The Supplemental Material contains the full M(B) curve ranging from -7 T to 7 T, 2023.
[34] R. Klingeler, J. Geck, R. Gross, L. Pinsard-Gaudart, A. Revcolevschi, S. Uhlenbruck, B. Büchner, Magnetism and the charge order transition in lightly doped $La_{1-x}Sr_xMnO_3$, Phys. Rev. B 65 (2002) 174404.